Near-field single-scattering calculations of aerosols: Sensitivity studies

We model the effects of the photosensitive parameters of aerosols on their optical properties to provide a solid framework for further experimental and theoretical studies. A spherical dust particle is used to study the effects of the ambient medium, size, surface roughness, wavelength, and imaginary part of the complex refractive index. Five Gaussian random spheres with different aspect ratios are simulated to study the dependence of aerosol light scattering properties on particle shape distribution. To investigate the influence of composition, we model two typical kaolinite-like particles(pure and composite) collected from Southwest Sahara, with 0% and 2% hematite at different mixing states. Using the method of discrete-dipole approximation in DDSCAT, a comparative study is performed with the Mueller matrix elements, scattering, absorption, extinction efficiencies, single scattering albedo, and linear depolarization ratio as indicators. For single, microscopic dust particles, near-field calculations are carried out. The results show that the intensity of backscattering and the scattering efficiency decreases in water compared to dry air. Light in the visible range is more efficient for aerosol scattering experiments. A small number of impurities in the sample will increase its absorbing properties, but in general, the scattering efficiencies strongly depend on the single-particle mixing state. Smaller particles with a diameter comparable to the wavelength of incident light show higher scattering efficiencies but lower backscattering intensities than larger particles, while surface roughness is shown to strongly alter the polarizability of the particle but has a negligible effect on its single-scattering albedo. Moreover, different shapes have a strong effect on the degree of linear polarization, but in general, using the spherical over elliptic shape model can underestimate the scattering efficiencies by up to 4%. Finally, variation in the imaginary part of the complex RI can underestimate the single scattering albedo by up to 35.8%.

Table S1. Parameter summary table and sensitivity analysis

Parameters		Models	Q_{ext}	Q_{abs}	Q_{scat}	ω	$S_{11}(180)$	$S_{22}(180)$	χ
Shape		GRS1	3.967	2.46E-19	3.967	∼1	1.128	6.31E-1	28.2E-2
(λ = 500nm)		GRS2	3.912	-2.0E-19	3.9137	∼1	1.678	1.654	0.72E-2
		GRS3	3.852	5.577E-21	3.852	∼1	1.709	1.689	0.59E-2
		GRS4	3.853	6.02E-19	3.853	∼1	1.755	1.739	0.46E-2
		GRS5	3.8067	2.462E-19	3.8068	∼1	2.416	2.416	0.00
Size parameter(x)		5.0	3.192	1.176	2.016	0.632	4.1392E-01	4.139E-1	0.0
(λ = 500nm)		17.6	2.301	1.132	1.169	0.51	2.247	2.247	0.0
Surface		Smooth	3.2995	6.7742E-2	3.2317	0.979	1.3209	1.321	∼0.0
roughness		Rough1	3.2995	6.762E-2	3.2319	0.979	1.2586	1.259	∼0.0
(λ = 500nm)		Rough2	3.2919	6.719E-2	3.2247	0.979	1.0137	1.013	∼0.0
Wavelength(nm)		300	2.0	2.14E-1	1.78	0.89	5.33	5.33	0.0
		500	3.91	1.2E-1	3.78	0.967	6.73	6.73	0.0
		700	3.95	8.64E-2	3.86	0.977	1.96	1.96	0.0
		1400	1.21	3.68E-2	1.17	0.967	4.0E-2	4.0E-2	0.0
Ambient		air	3.91	1.26E-1	3.78	0.967	6.74	6.74	0.0
(λ = 500nm)		water	1.08	7.4E-2	1.01	0.93	7.13E-2	7.13E-2	0.0
Particle		0.0015	3.943	4.098E-2	3.902	0.989	7.658	7.658	0.0
Im(RI)		0.0048	3.911	1.265E-1	3.784	0.967	6.738	6.738	0.0
(λ = 500nm)		0.01	3.862	2.494E-1	3.612	0.935	5.508	5.508	0.0
		0.1	3.192	1.176	2.016	0.631	4.139E-1	4.139E-1	0.0
Composition		Pure kaolinite	4.239	-5.95E-19	4.239	1	4.118	3.95	2.1E-2
(λ = 380 nm)		Random	4.228	1.917E-2	4.209	0.995	4.85	4.635	2.26E-2
		Homogeneous	4,23	2.28E-2	4.21	0.995	5.154	4.924	2.28E-2
		Sur1	4.35	1.62E-2	4.34	0.997	5.05	4.85	2.0E-2
	Asymmetric	Sur2	4.33	5.58E-2	4.276	0.987	7.58	7.21	2.5E-2
	Distribution	Sur3	4.34	4.63E-2	4.29	0.988	5.95	5.72	1.97E-2
	(Surface incursion)	Sur4	4.36	5.42E-2	4.3	0.986	6.47	6.05	3.35E-2
		Mean	4.343	5.21E-2	4.289	0.987	6.667	6.327	2.61E-2
		Stdv	0.015	0.005	0.012	0.001	0.833	0.783	0.007
	Asymmetric	Lump1	4.08	6.5E-2	4.016	0.984	4.23	2.48	2.6E-1
	Distribution	Lump2	4.027	8.456E-2	3.943	0.979	3.455	2.470	1.66E-1
	(Lump incursion)	Lump3	3.78	8.37E-2	3.695	0.978	3.628	3.437	2.7E-2
		Mean	3.962	7.78E-2	3.885	0.980	3.771	2.796	1.51E-1
		Stdv	0.160	0.011	0.168	0.003	0.407	0.555	0.117
Composition		Pure kaolinite	3.852	5.577E-21	3.852	1	1.709	1.689	5.88E-3
(λ = 500 nm)		Random	3.956	1.219E-2	3.944	0.997	1.895	1.87	5.31E-3
		Homogeneous	4.01	1.51E-2	3.997	0.997	1.98	1.95	7.6E-3
		Sur1	3.97	1.01E-2	3.963	0.998	1.95	1.925	6.45E-3
	Asymmetric	Sur2	4.03	3.28E-2	3.996	0.991	2.463	2.40	1.3E-2
	Distribution	Sur3	4.03	2.83E-2	3.998	0.992	2.28	2.237	9.5E-3
	(Surface incursion)	Sur4	4.04	3.05E-2	4.00	0.99	2.127	2.079	1.14E-2
		Mean	4.033	3.05E-2	3.998	0.991	2.29	2.239	1.13E-2
		Stdv	0.006	0.002	0.002	0.001	0.168	0.161	0.002
	Asymmetric	Lump1	3.97	5.27E-2	3.916	0.986	1.653	1.549	3.24E-2
	Distribution	Lump2	4.025	6.864E-2	3.956	0.983	1.639	1.426	6.95E-2
	(Lump incursion)	Lump3	3.52	6.524E-2	3.454	0.981	1.26	1.22	1.6E-2
		Mean	3.838	6.22E-2	3.775	0.983	1.517	1.398	3.93E-2
		Stdv	0.277	0.008	0.279	0.003	0.223	0.166	0.027
Composition		Pure kaolinite	2.768	1.288E-20	2.768	1	7.662E-1	7.628E-1	2.22E-3
(λ = 650 nm)		Random	2.934	8.62E-3	2.926	0.997	7.517E-1	7.48E-1	2.67E-3
		Homogeneous	3.02	1.1E-2	3.01	0.0997	7.49E-1	7.45E-1	3.34E-3
		Sur1	2.899	7.2E-3	2.89	0.997	7.12E-1	7.08E-1	2.8E-3
	Asymmetric	Sur2	2.98	2.23E-2	2.96	0.993	6.51E-1	6.41E-1	7.74E-3
	Distribution	Sur3	2.97	1.91E-2	2.95	0.993	6.7E-1	6.61E-1	6.76E-3
	(Surface incursion)	Sur4	2.98	2.01E-2	2.96	0.993	6.64E-1	6.59E-1	4.96E-3
		Mean	2.977	2.05E-2	2.957	0.993	6.62E-1	6.54E-1	6.49E-3
		Stdv	0.006	0.002	0.006	0	0.009	0.011	0.001
	Asymmetric	Lump1	2.992	2.249E-2	2.969	0.992	7.98E-1	7.912E-1	4.2E-3
	Distribution	Lump2	3.015	2.374E-2	2.99	0.992	7.357E-1	7.277E-1	5.46E-3
	(Lump incursion)	Lump3	3.057	3.58E-2	3.021	0.988	4.656E-1	4.563E-1	1.1E-2
		Mean	3.021	2.73E-2	2.993	0.991	6.66E-1	6.58E-1	6.89E-3
		Stdv	0.033	0.007	0.026	0.002	0.18	0.178	0.004

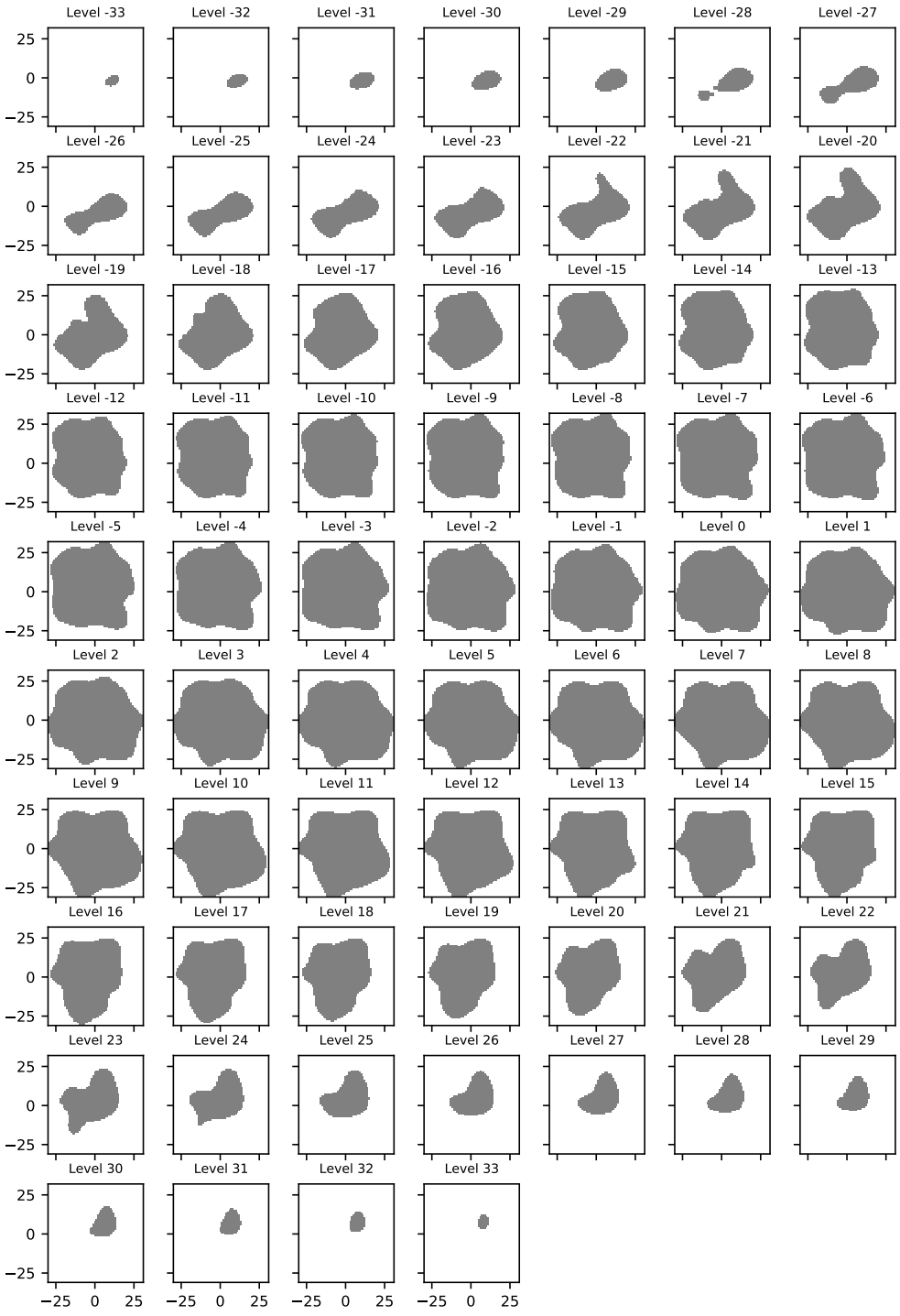

Fig. S1. Tomography images when the particle in Figure 10b is sliced along the z-axis in the x-y plane for the pure kaolinite particle(Pure).

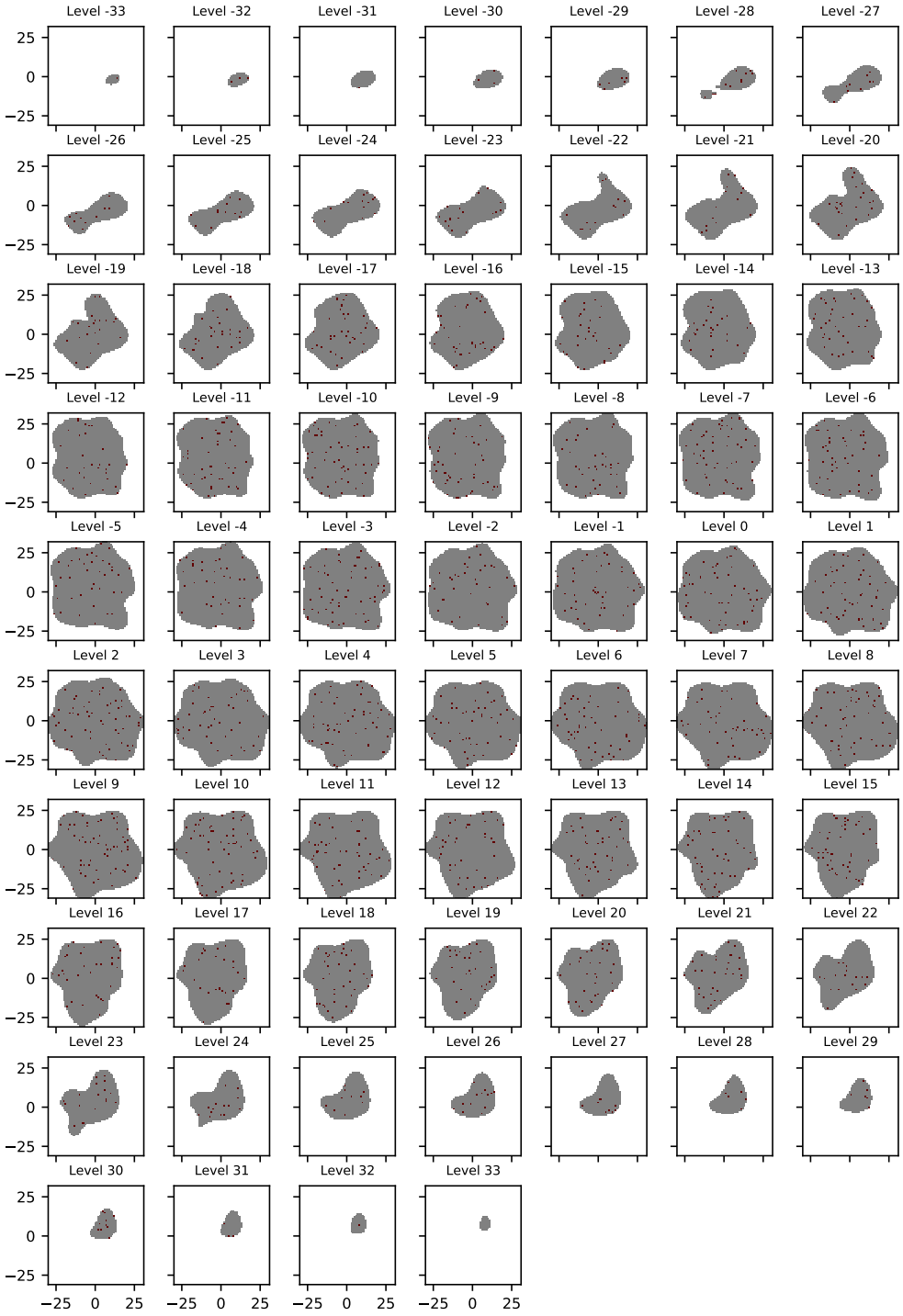

Fig. S2. Tomography images when the particle in Figure 10b is sliced along the z-axis in the x-y plane to show the location of the pure dipole particles(grey) and impurities(dark red) for the random model distribution of impurities(Random).

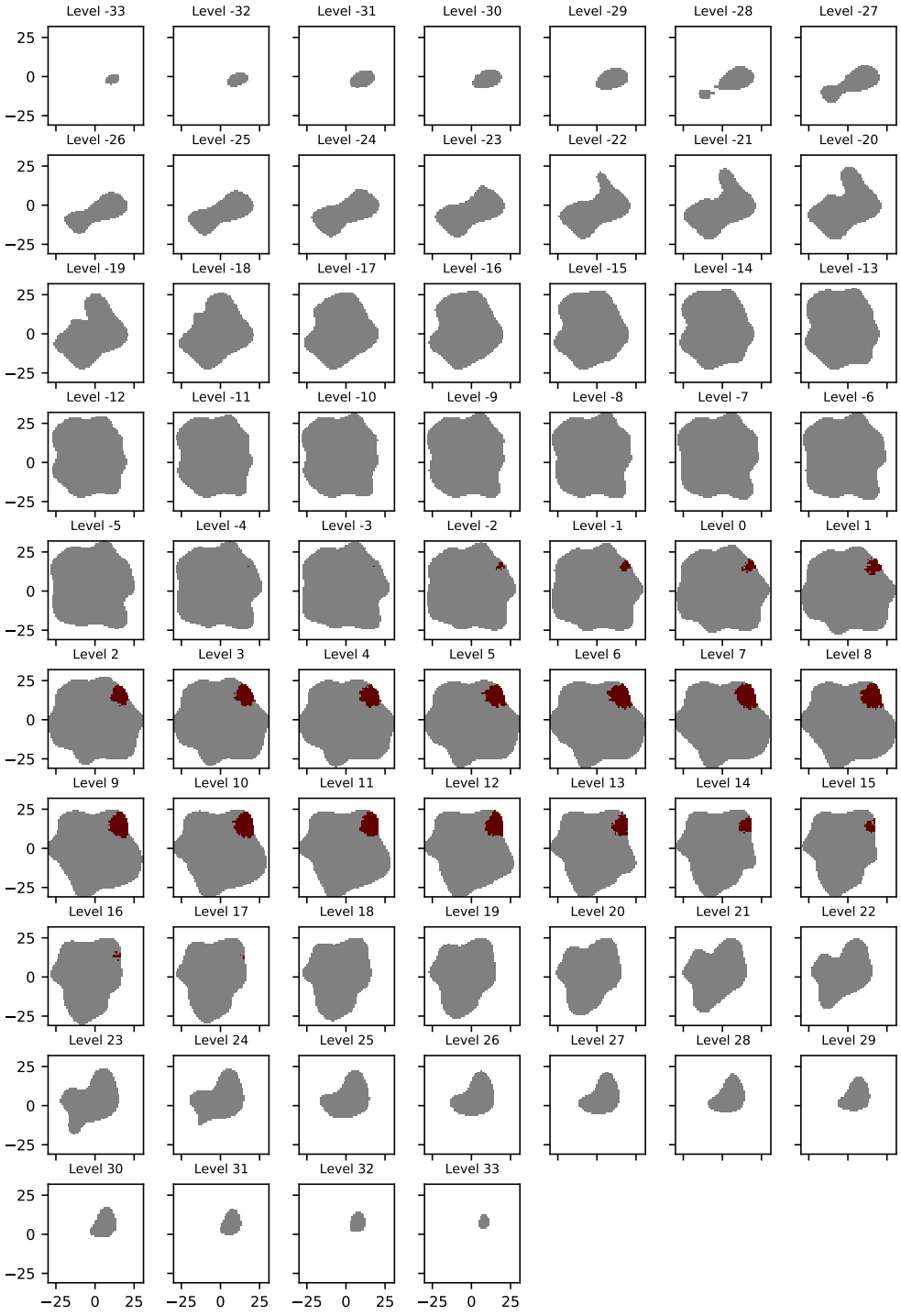

Fig. S3. Tomography images when the particle in Figure 10b is sliced along the z-axis in the x-y plane to show the location of the pure dipole particles(grey) and impurities(dark red). Here, the lump is located at the topmost surface of the particle (Lump1).

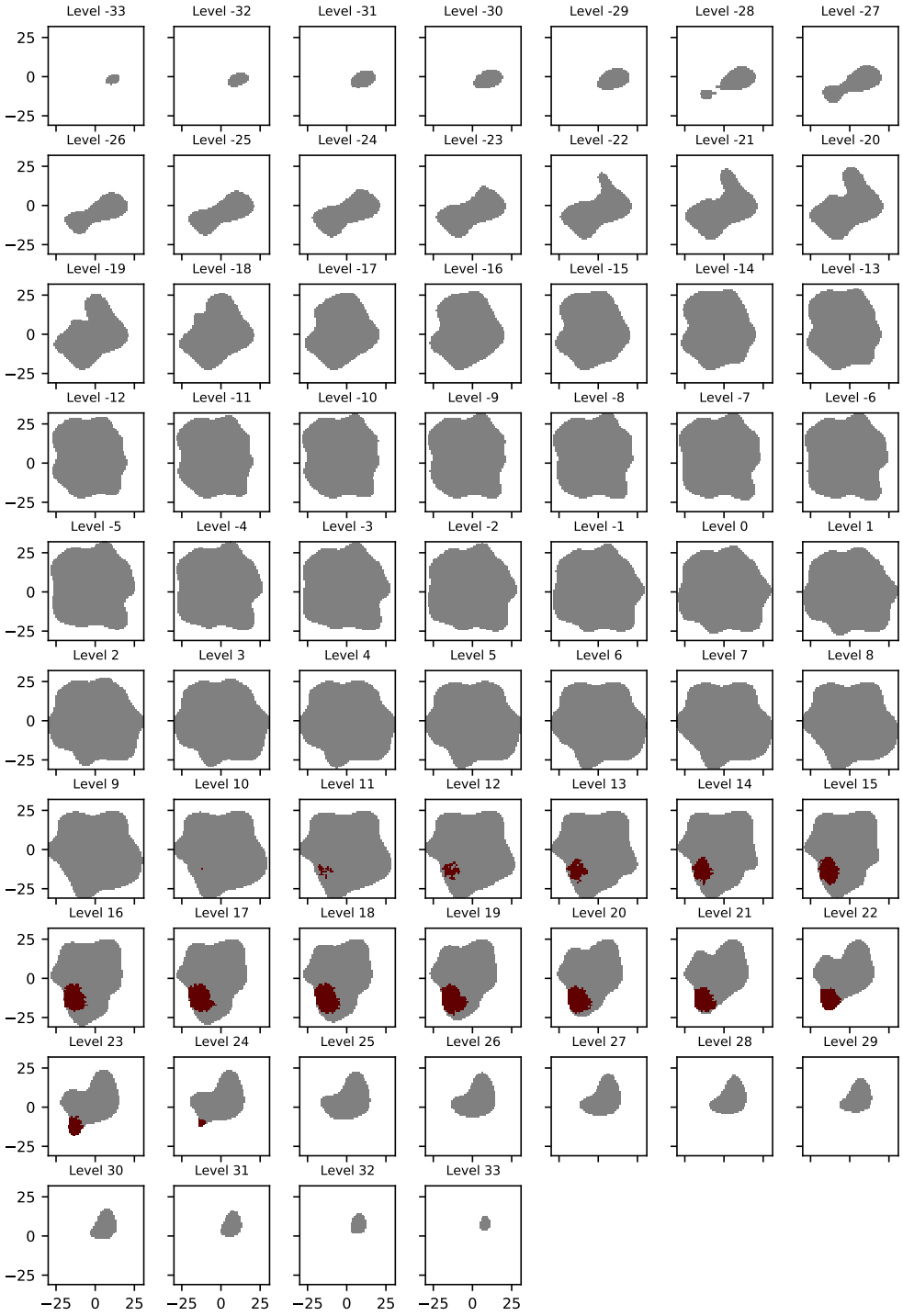

Fig. S4. Tomography images when the particle in Figure 10b is sliced along the z-axis in the x-y plane to show the location of the pure dipole particles(grey) and impurities(dark red). Here, the lump is located at the bottommost surface of the particle(Lump2).

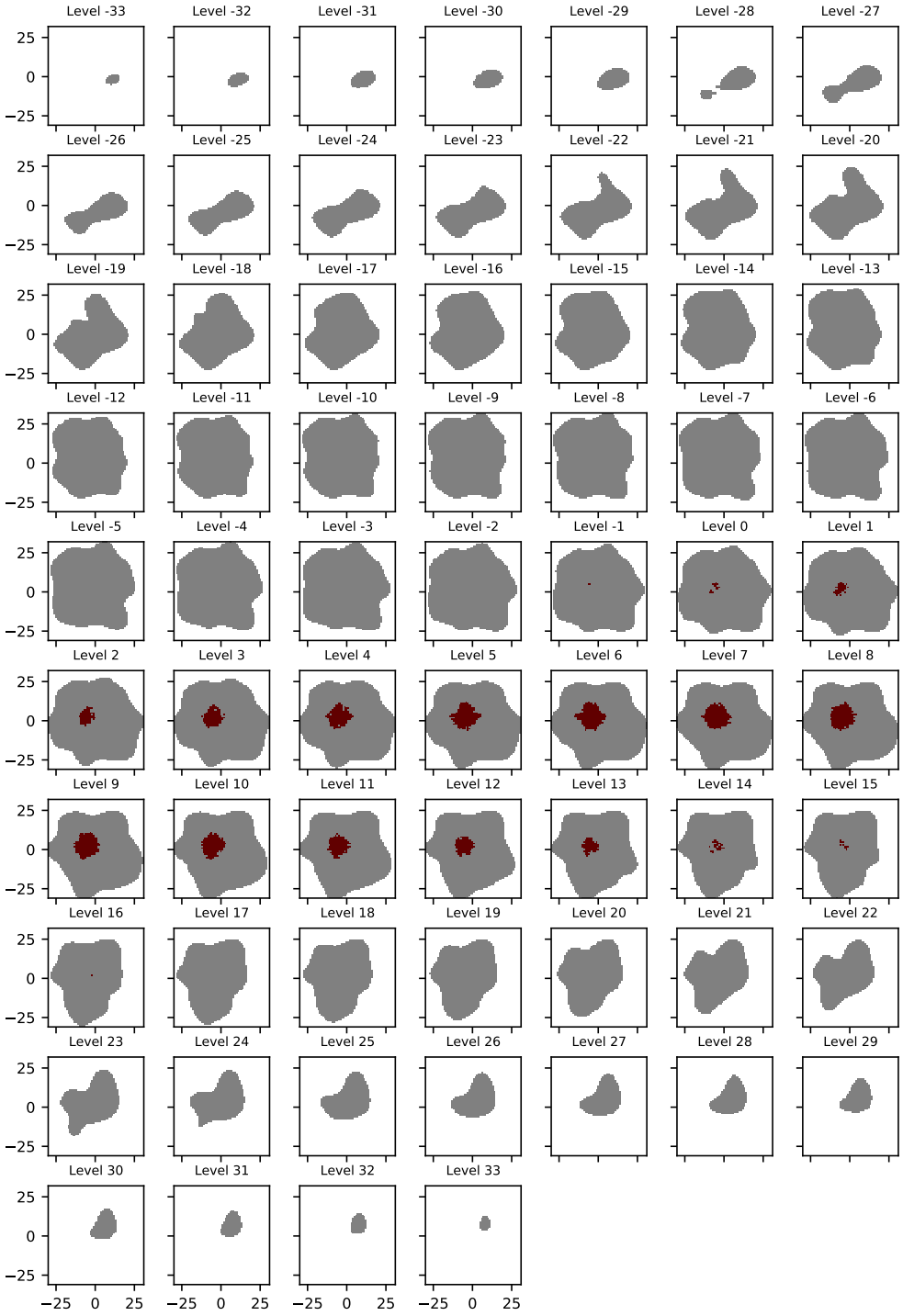

Fig. S5. Tomography images when the particle in Figure 10b are sliced along the z-axis in the x-y plane to show the location of the pure dipole particles(grey) and impurities(dark red). Here, the lump is located near the center of the particle(Lump3).

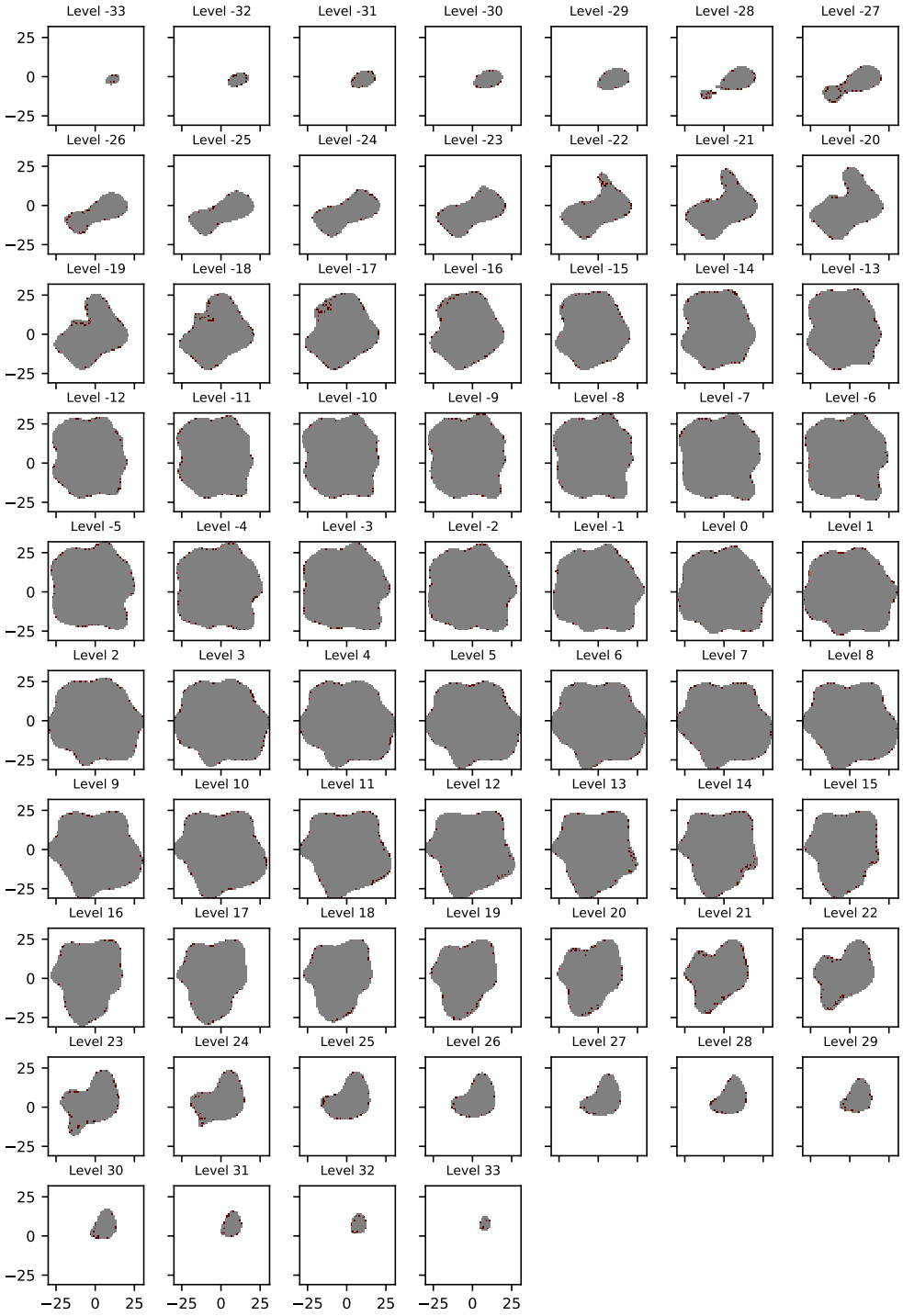

Fig. S6. Tomography images when the particle in Figure 10b is sliced along the z-axis in the x-y plane to show the location of the pure dipole particles(grey) and impurities(dark red). Here, the uniformly distributed surface incursion is shown.

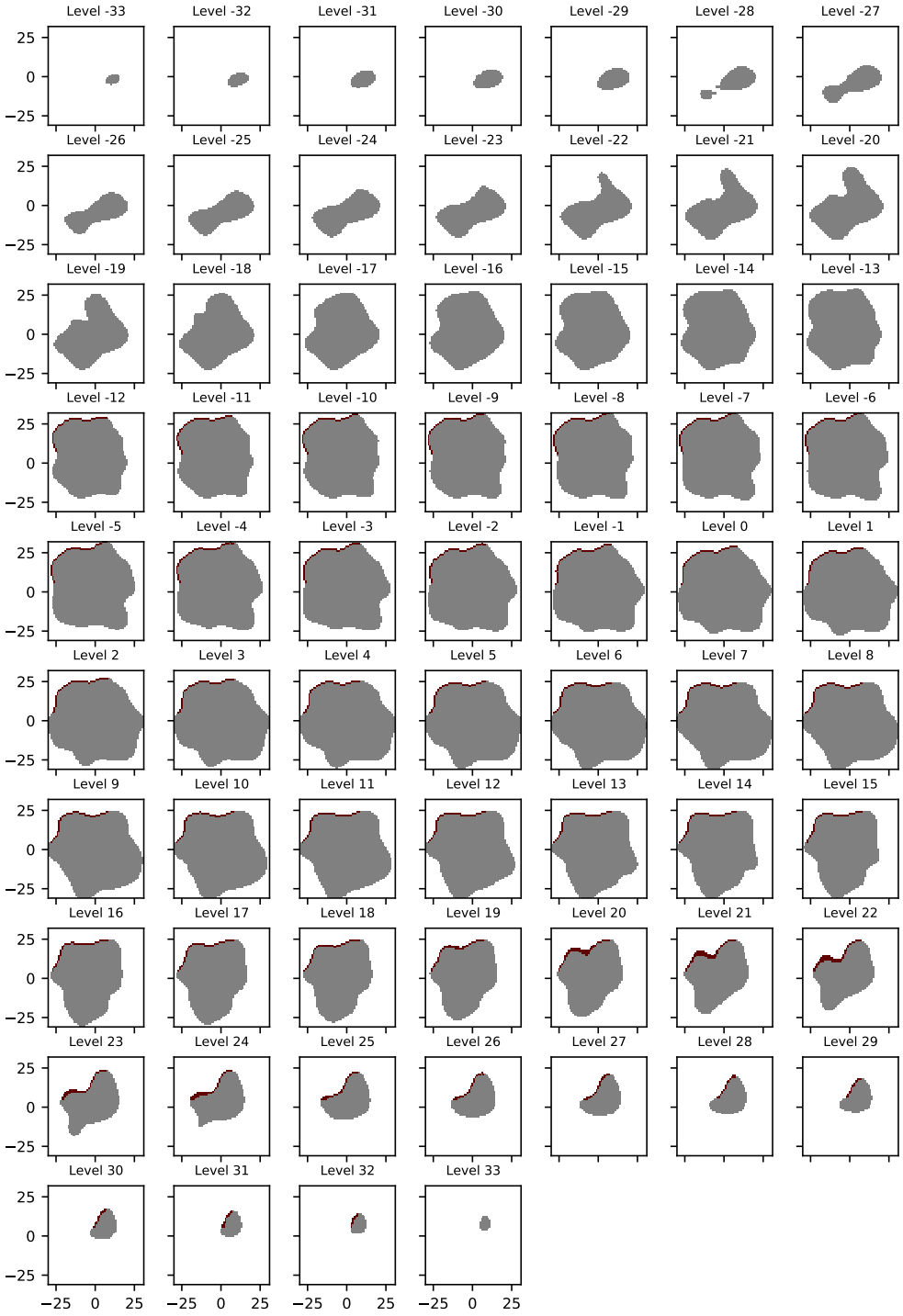

Fig. S7. Tomography images when the particle in Figure 10b is sliced along the z-axis in the x-y plane to show the location of the pure dipole particles(grey) and impurities(dark red). Here, the asymmetric distributed surface incursion is shown.

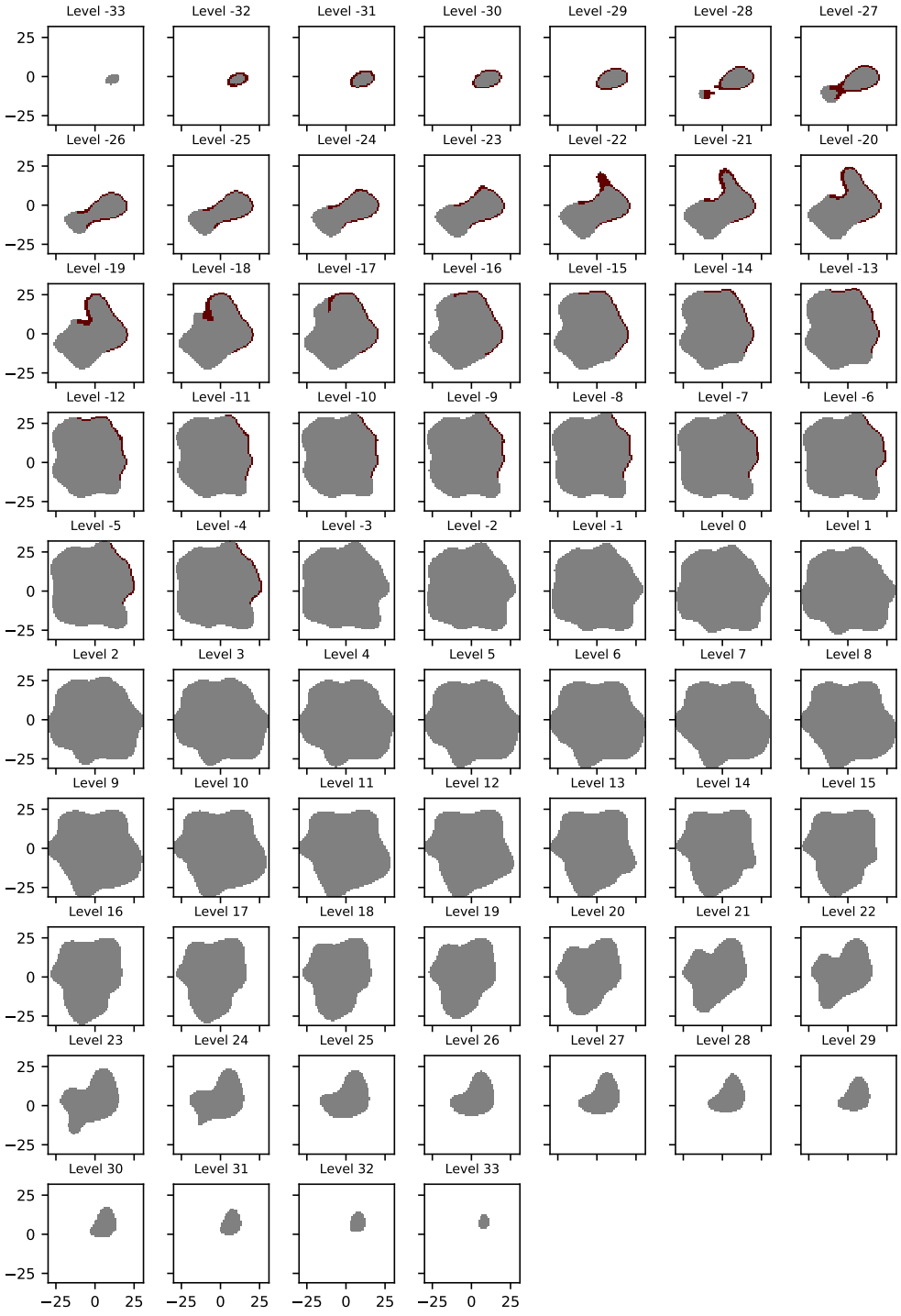

Fig. S8. Tomography images when the particle in Figure 10b is sliced along the z-axis in the x-y plane to show the location of the pure dipole particles(grey) and impurities(dark red). Here, the asymmetric distributed surface incursion is shown.

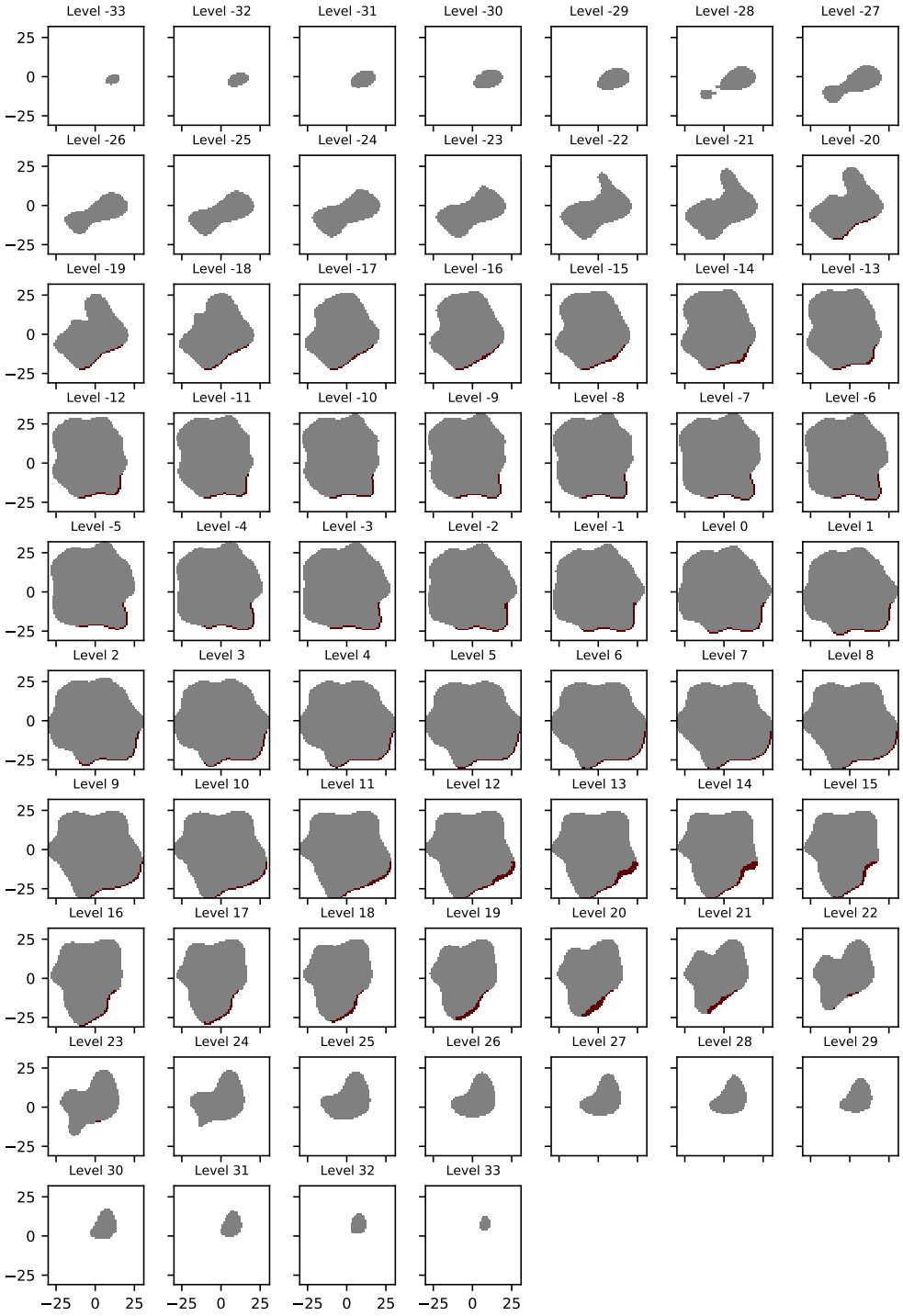

Fig. S9. Tomography images when the particle in Figure 10 is sliced along the z-axis in the x-y plane to show the location of the pure dipole particles(grey) and impurities(dark red). Here, the asymmetric distributed surface incursion is shown.

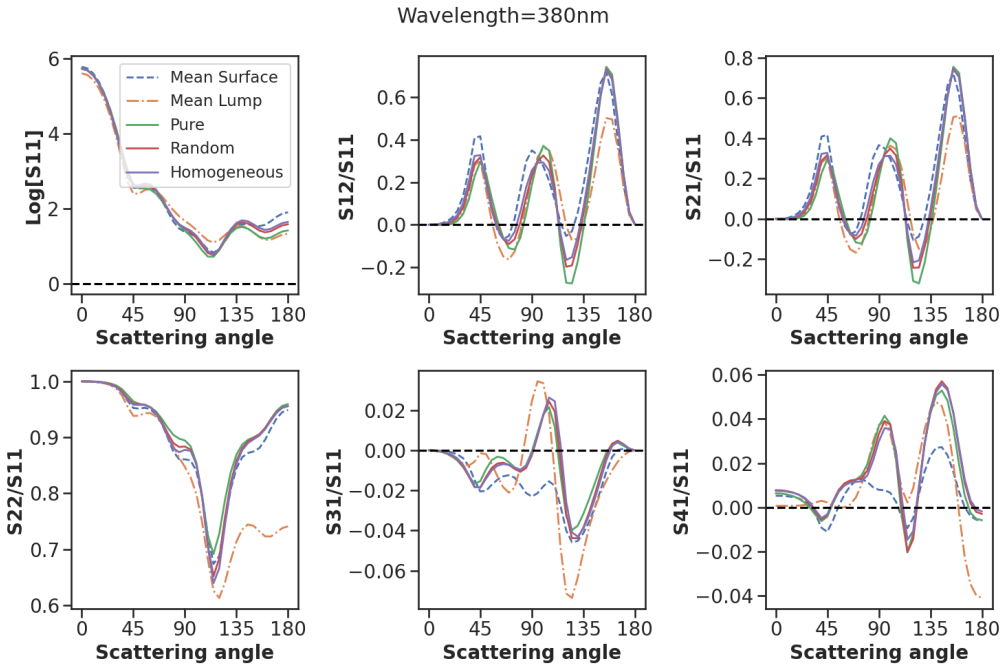

Fig. S10. Simulated single-scattering Mueller matrix elements for the aerosol particle models shown in Fig 11 with different chemical compositions and mixing states. The averages of the lumps and surface incursion models have been plotted and compared with other models. The method of Orientational Averaging has been used with the scattering computation averaged over 48 target orientations and 2 incident polarizations. The plot for visible light of wavelength $\lambda = 380nm$ has been used here where the complex refractive index of Kaolinite is $m_k = 1.562 + 0.00i$ while that of Hematite is $m_h = 3.1020 + 0.0925i$.

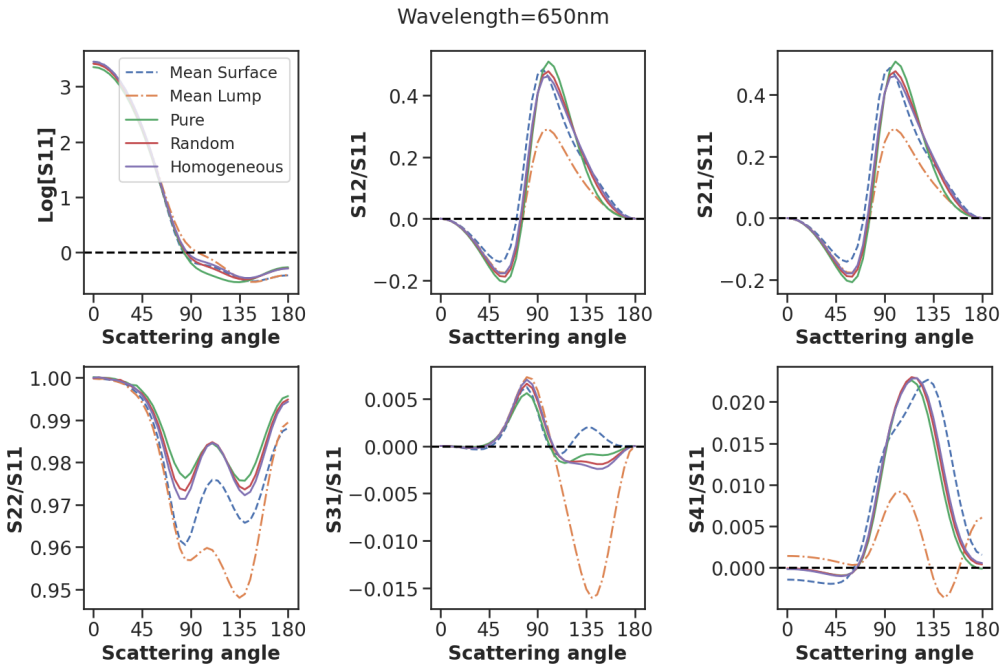

Fig. S11. Simulated single-scattering Mueller matrix elements for the aerosol particle models shown in Fig 11 with different chemical compositions and mixing states. The averages of the lumps and surface incursion models have been plotted and compared with other models. The method of Orientational Averaging has been used with the scattering computation averaged over 48 target orientations and 2 incident polarizations. The plot for visible light of wavelength $\lambda = 650nm$ has been used here where the complex refractive index of Kaolinite is $m_k = 1.562 + 0.00i$ while that of Hematite is $m_h = 3.1020 + 0.0925i$.